RSC Advances

PAPER

View Article Online
View Journal | View Issue

Check for updates

Cite this: *RSC Adv.*, 2020, **10**, 9814

Defective S/N co-doped carbon cloth *via* a one-step process for effective electroreduction of nitrogen to ammonia†

Shaoan Cheng,* Chaochao Li, Zhen Yu, Yi Sun, Longxin Li and Jiawei Yang

The electroreduction of nitrogen (N_2) has gained increasing attention as a promising route to achieve green and sustainable ammonia (NH_3) production. However, the construction of an active and durable electrocatalyst for N_2 reduction reaction (NRR) remains a significant challenge. Herein, we, for the first time, report that S/N co-doped carbon cloth (CC) with abundant defects can serve as an efficient NRR electrocatalyst at ambient conditions. The S/N co-doped CC was prepared through a novel one-step method by using ammonium persulfate (APS) as the source of nitrogen and sulfur. The catalyst prepared at 800 °C (CC-APS 800) showed abundant defects and heteroatoms as the active and stable electrocatalytic sites for NH_3 electrosynthesis. Based on this, a sizeable NH_3 yield of 9.87 × 10^{-10} mol s^{-1} cm^{-2} and high faradaic efficiency of 8.11% were obtained in 0.05 M H_2SO_4 at −0.3 V (*vs.* reversible hydrogen electrode, RHE), respectively. Furthermore, the electrocatalytic mechanism on CC-APS 800 was elucidated using the electrochemical *in situ* Fourier transform infrared technique, and follows an associative reaction pathway. Our work would provide a new guideline for designing metal-free self-standing electrocatalysts for the NRR and other applications.

Received 7th January 2020
Accepted 24th February 2020

DOI: 10.1039/d0ra00155d

rsc.li/rsc-advances

Open Access Article. Published on 06 March 2020. Downloaded on 5/9/2026 12:36:21 PM.
This article is licensed under a Creative Commons Attribution-NonCommercial 3.0 Unported Licence.

Introduction

As an active form of nitrogen (N_2), ammonia (NH_3) has become an indispensable ingredient of the modern agriculture and chemistry industry.[1] However, the industrialized Haber–Bosch (H–B) method for modern ammonia synthesis requires high temperature (~500 °C) and high pressure (20–40 MPa), and uses H_2 as reductant (from steam reforming of natural gas).[2] As a result, the H–B method contributes to 1–2% of the global energy consumption and over 300 million tons of CO_2 emission per year. Therefore, given the serious environmental concerns and climate change, there is an urgent need to explore green and sustainable alternatives to the H–B method.

The technique of nitrogen reduction reaction (NRR) has attracted increasing attention with less energy consumption, little climate change, and low cost. On the surface of the catalyst, the absorbed N_2 molecules will break or dissociate on the active sites, further combine with the protons, and finally form the NH_3 with the cooperation of electrons. ($N_{2(g)} + 6H_{(aq)}{}^{+}$ $[8H_{(aq)}{}^{+}] + 6e^{-} \xrightarrow{\text{normal perssure and temperature}} 2NH_{3(aq)}[2NH_{4(aq)}{}^{+}]$). Up to now, a large variety of electrocatalysts based on noble metals (such as Au,[3] Pt,[4] Ru,[5] Ag,[6] *etc.*) and transition metals (such as Co,[7] Sn,[8] Mn,[9] Ti,[10] Mo,[11] V,[12] Fe,[13] *etc.*) has been developed for ammonia electrosynthesis. However, the practical utilization of these metal-based catalysts was often limited by the material cost and environmental impact. Therefore, developing an efficient and durable metal-free catalyst has been regarded as one of the most potential breakthroughs for the NRR technique.

As an earth-abundant metal-free catalyst, carbon-based electrocatalysts are promising for NRR owing to their unique superiorities on the electric conductivity, chemical durability, surface area, and electronic structure.[5] However, to better weaken the strong N≡N bonding (~945.6 kJ mol^{-1}), the modulation of the electronic structure of carbon is very important, and the method of heteroatom doping has been proved as a reliable tool.[14] For recent years, various heteroatoms owning similar electronic orbits to carbon (such as nitrogen,[15] sulfur,[16] fluorine,[17] and boron[18]) have been investigated to regulate the electronic configuration of carbon, and thus promote the NRR performance. Furthermore, it is considered that co-doping carbon materials with two kinds of heteroatoms may co-activate the adjacent C atom and construct some unexpected electronic structures, which usually provides much more active sites than that of one heteroatom doping, and enhances the NRR performance eventually. However, dual-dopant pairs reported in co-doped carbon materials for NRR

State Key Laboratory of Clean Energy Utilization, Department of Energy Engineering, Zhejiang University, Hangzhou 310027, PR China. E-mail: shaoancheng@zju.edu.cn

† Electronic supplementary information (ESI) available: Experimental details, the elemental composition of the catalysts based on the XPS spectra, the schematic illustration of the fabrication of CC-APS 800; TGA curves of CC, APS, and CC-APS composite; Raman and FTIR spectra, photos of contact angle tests, SEM and EDS images, CV and LSV curves of the samples, UV-vis absorption and calibration curves of NH_3–N and $N_2H_4{\cdot}H_2O$, time-dependent current density curves and NH_3 yield. See DOI: 10.1039/d0ra00155d

This journal is © The Royal Society of Chemistry 2020

Open Access Article. Published on 06 March 2020. Downloaded on 5/9/2026 12:36:21 PM.
This article is licensed under a Creative Commons Attribution-NonCommercial 3.0 Unported Licence.

are merely restricted to N–P[19,20] and N–B[21,22] couples. Sulfur/nitrogen co-doped carbon has gained remarkable progress in multiple electrocatalysis fields, including oxygen reduction reaction (ORR),[23] oxygen evolution reaction (OER),[24] and hydrogen evolution reaction (HER).[25] Recent literatures have reported the theoretical calculation results of the S/N-codoped graphene as the catalyst for NRR.[26,27] Due to the higher electronegativity of N (3.04) and S (2.58) relative to C (2.55), the N/S dopants can induce the positive charge densities on the adjacent carbon atoms, which favor the adsorption of N_2. Thus, the N/S-adjacent carbon atoms act as the active sites for N_2 adsorption and subsequent activation. According to the DFT results, the N_2 adsorption energy of S/N-codoped carbon is predicted to be 0.42 eV, which is much higher than those of N-doped carbon (0.31 eV) and S-doped carbon (0.19 eV). This suggests that S/N-codoping can co-activate the neighboring C atoms to enhance the N_2 adsorption. Nevertheless, the performance and reaction mechanism of S/N co-doped carbon for N_2 electroreduction remains unexplored.

In this work, we present, for the first time, a defective S/N co-doped carbon cloth (CC) for electrocatalytic N_2 fixation. The S/N co-doped CC with abundant defects was prepared *via* a facile one-step thermochemical treatment with ammonium persulfate (APS) as the dopant source of N and S. The NRR performance of the resulting catalyst was investigated at a low potential of −0.3 V *vs.* RHE. The reaction pathway of NRR was pursued through the electrochemical *in situ* Fourier transform infrared (FTIR) technique.

Results and discussion

Defective S/N co-doped CC was prepared *via* a facile thermochemical treatment (Fig. 1a, details in ESI†) on commercial CC. As a common supporting material for electrocatalysis, the self-standing CC is binder-free, chemical stable, and cost-effective. In this novel process, APS is reported as the nitrogen and sulfur source for the first time. As-prepared samples treated with APS under different temperatures were denoted as CC-APS *X* (*X* represents the temperature of 200, 400, 600, or 800 °C, respectively). The thermal interaction between APS and CC was determined through thermogravimetric analysis (TGA) measurements. As shown in Fig. S1,† the mass of APS decreases sharply to zero at about 455 °C, which implies that APS has been completely pyrolyzed into gases (including NH_3, SO_2, SO_3, H_2O, and O_2).[28] With the temperature further increasing, the mass of APS-CC blend presents another noticeable decrease at 625 °C, while that of CC showed no obvious change during the whole process. This result is attributed to the further reaction of CC with those pyrolysis gases, which probably leads to the introduction of heteroatoms.

The SEM images also show that more and more corrosion has been made on the CC surface, with the treating temperature increasing (illustrations in Fig. 1b–f). Particularly, complex 3D nanostructures composed of irregular holes and grooves have been dramatically formed on the surface of CC-APS 800. The transmission electron microscopy (TEM) images of the treated CCs (Fig. 1g–k) demonstrate clearly that the disorder of lattice fringes in the samples has been aggravated as the treating temperature increases. The distortion of the atomic arrangement possibly reflecting the abundant doping of heteroatoms or carbon vacancies.[29,30] Also, some ultra-thin carbon layers have been formed on the edge of the carbon fiber after the heating process. Those irregular carbon nanosheets may provide rich active sites for nitrogen absorption and activation.[31] We also investigated the treated CC obtained at 900 °C; however, the as-fabricated sample lost 76% of its original mass, and finally became too fragile to support itself as an electrode for electrocatalysis.

X-ray photoelectron spectroscopy (XPS) analysis was employed to explore the elementary configuration and chemical state of as-prepared CC catalysts. As shown in Fig. 2a, the XPS overall spectra of treated CCs depicts obvious S (∼164.8 eV), C (∼285.2 eV), N (∼400.0 eV), and O (∼531.5 eV) peaks,[32] while that of the pristine CC only shows C, O, and weak N peaks. Moreover, the content of S and N increases with the temperature increasing (Table S1, Fig. S2†). As a result, CC-APS 800 shows the maximum atomic ratio of N/C and S/C of 8.23 at% and 2.51 at%, respectively. Accordingly, C–S (281.2 eV) and C–N (282.0 eV) peaks can be found in the C 1s spectra (Fig. 2b), confirming the resultful doping of S and N.[33] Moreover, N 1s spectrum (Fig. 2c) of CC-APS 800 can be resolved into three peaks at 398.6, 399.8, and 401.0 eV, which are assigned to pyridinic N (24.97 at%), pyrrolic N (39.02 at%), and graphitic N (36.01 at%), respectively.[29] Pyridinic and pyrrolic N occupies 63.99 at% of the total amount of N in CC-APS 800, producing massive catalytic sites for N_2 electroreduction.[15,34] As shown in Fig. 2d, the peaks of 164.0 eV and 168.4 eV in the S 2p spectrum are assigned to C–S–C and C–SO_x–C ($x = 2, 3, 4$), respectively.[35] The strong signal of thiophene-S indicates that the incorporated S atoms are mainly bonded with two C atoms at the edges or defects of disordered carbon networks, which are chemically active sites for electroreduction reaction.[36] The surface elementary compositions were further analyzed using energy dispersive spectrum (EDS). The EDS elemental mapping for CC-APS 800 (Fig. S3†) indicates that both N and S atoms have been evenly introduced into the resulting carbon cloth with considerable quantities.

The isothermal N_2 adsorption–desorption test was utilized to study the N_2 adsorption ability and pore properties of the catalyst surface. CC-APS 800 presents a type-IV isotherm with an H2 shaped hysteresis loop in the p/p_0 range of 0.4–0.8 (Fig. 3a), usually indicating massive mesoporous structures on the surface.[37] As calculated by the BJH (Barrett–Joyner–Halenda) method, CC-APS 800 exhibits dominant mesopores centered at ∼3.5 nm and micropores concentrated at ∼1.7 nm, while nearly no pore structure is observed for the pristine CC (Fig. 3b). Correspondingly, CC-APS 800 presents a large surface area of 610.26 $m^2\ g^{-1}$ as calculated through BET (Brunauer–Emmett–Teller) method, while the pristine CC only has a surface area of 1.19 $m^2\ g^{-1}$. Furthermore, the electrochemical active surface area (ECSA) of the catalysts was measured by cyclic voltammetry (Fig. S4†).[38] The ECSA of CC increases from 0.0042 to 1.7754 mF cm^{-2} after the calcination at 800 °C, demonstrating the generation of massive electrochemically active sites. Besides the large

Open Access Article. Published on 06 March 2020. Downloaded on 5/9/2026 12:36:21 PM.
This article is licensed under a Creative Commons Attribution-NonCommercial 3.0 Unported Licence.

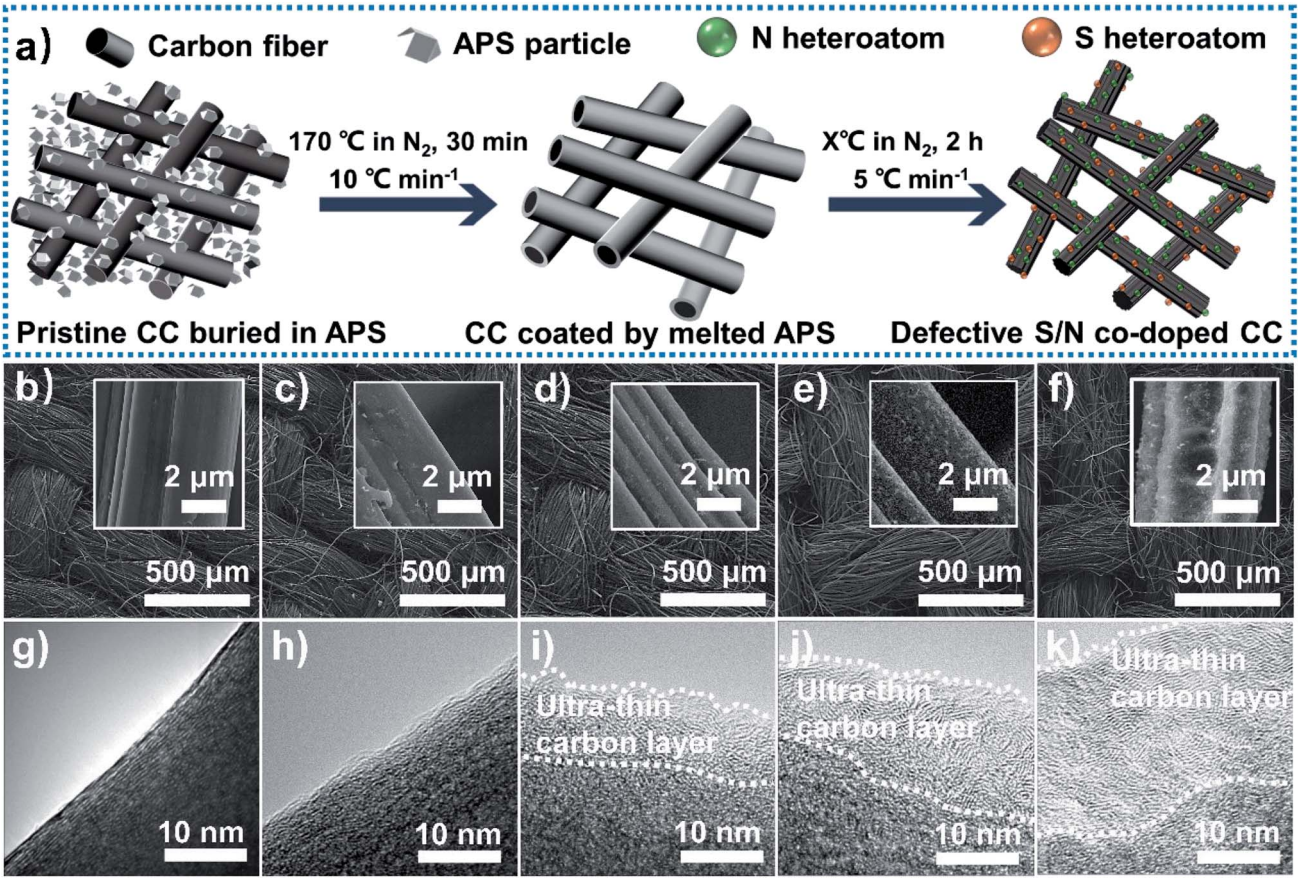

Fig. 1 (a) Schematic illustration of the synthesis process of the defective S/N co-doped CC. Through a similar process with different treating temperatures (X °C), CC-APS X (X = 200, 400, 600, and 800, respectively) can be easily fabricated. SEM images of (b) pristine CC, (c) CC-APS 200, (d) CC-APS 400, (e) CC-APS 600, and (f) CC-APS 800. TEM images of (g) pristine CC, (h) CC-APS 200, (i) CC-APS 400, (j) CC-APS 600, and (k) CC-APS 800.

surface area, according to the contact-angle test results, the change of surface wettability also accounts for the improved ECSA (Fig. S5†). By treating CC with APS at high temperature (>400 °C), the surface contact angle increases form ~127.4° to ~180°. The surface hydrophilicity is significantly enhanced, which constructs the fast supply of hydrogen for hydrogenation reactions.[39] The FTIR spectra (Fig. S6†) revealed the generation of abundant N- and S-containing functional groups on the surface of CC-APS 800. Those functional groups with strong polarity mainly endow CC-APS 800 with a super-hydrophilic surface.[40] Temperature-programmed desorption (TPD) has been further carried out to investigate the capability of S/N-codoped carbon cloth for N_2 adsorption (Fig. S9†), which is a prerequisite step of NRR. As the result, the pristine CC performed very weak physisorption (at about 100 °C) and chemisorption (at about 335 °C) of N_2.[41,42] However, for the S/N-codoped carbon cloth (CC-APS 800), the physisorption and chemisorption were significantly enhanced, suggesting that sulfur and nitrogen dopants induce the physical and chemical adsorption sites for N_2 molecules. As a summary, the supplement of N_2 gas (nitrogen source), water (hydrogen source), and electrons (energy source) are dramatically enhanced on the triple-phase boundary on CC-APS 800.

The Raman spectra were investigated to characterize the defects of CC-APS X (Fig. 3c). The G band corresponding to 1530–1660 cm^{-1} was attributed to graphitic in-plane vibrations with E_{2g} symmetry, whereas the D band indexed to 1270–1430 cm^{-1} generally was ascribed to the presence of defects and disorder in the carbon atomic array. These defects were probably caused by the in-plane substitutional heteroatoms.[43] Notably, both the G band and D band shifted to higher wavenumbers after the thermochemical treatment, which probably resulted from the etching of graphite crystallites and the electron-cloud migration caused by doping heteroatoms.[44] The intensity ratio of the D band and G band (I_D/I_G) is a credible indicator for the defect extent in carbon materials.[45] CC-APS 800 showed the higher I_D/I_G of 1.15 than those of other samples, which implies the more abundant defects existing. These facts usually contribute to the superior NRR activity.[29,30,46] In the XRD patterns of CC-APS X (Fig. 3d), the typical diffraction peaks at 25.2° and 43.6° could be well ascribed to the (002) and (101) planes of the hexagonal graphite (JCPDS no.75-1621), respectively. Notably, the diffraction peaks of CC-APS 800 are dramatically lower and broader than other CC-APS X, which demonstrated a sharp transformation from graphitic to amorphous carbon in CC-APS X. This transformation was probably

 This journal is © The Royal Society of Chemistry 2020

Open Access Article. Published on 06 March 2020. Downloaded on 5/9/2026 12:36:21 PM.
This article is licensed under a Creative Commons Attribution-NonCommercial 3.0 Unported Licence.

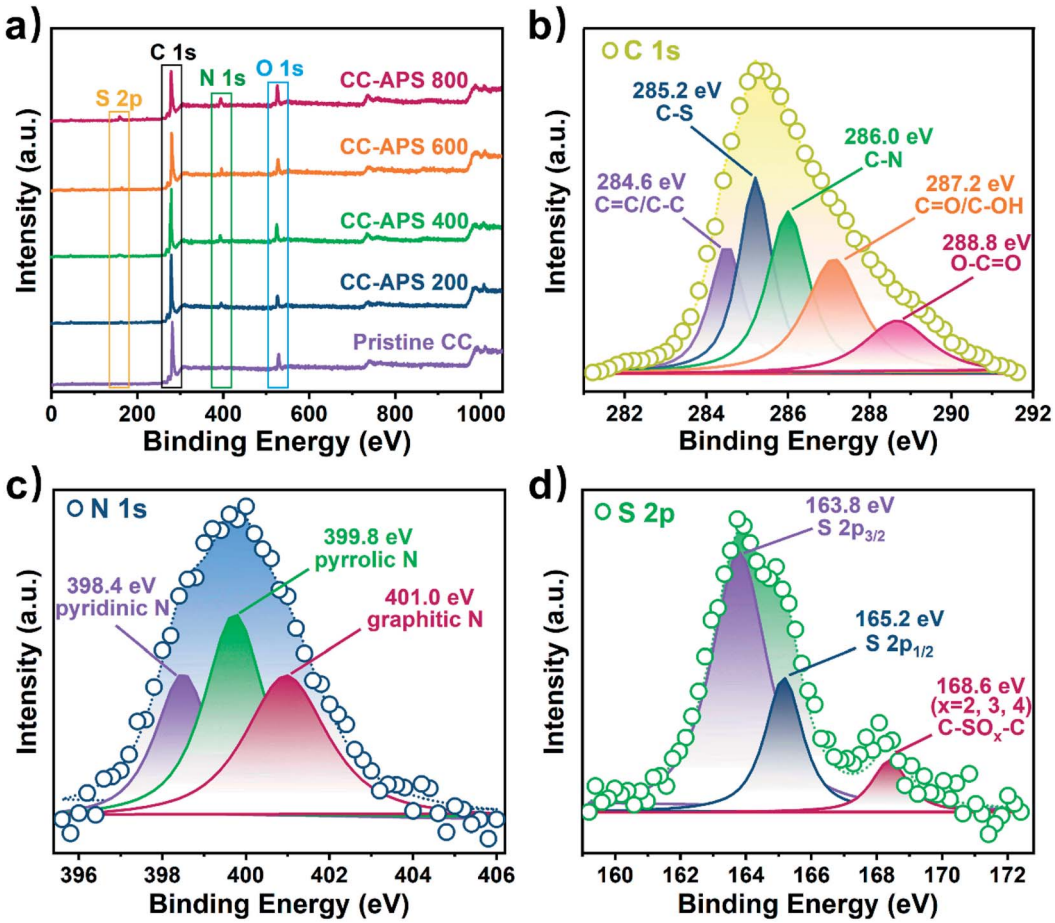

Fig. 2 (a) XPS overall spectra of the pristine CC, CC-APS 200, CC-APS 400, CC-APS 600, and CC-APS 800. XPS spectra of (b) C 1s, (c) N 1s, and (d) S 2p of CC-APS 800.

caused by the etching and doping effects of 800 °C calcination, which was also consistent with the Raman results.

To investigate the performance of CC-APS *X* quantitatively, a typical three-electrode system established in a typical H-type reactor[47] was used to measure the NH_3 yield (details in ESI†). To avoid any trace amount of N-containing contaminant, the catalysts, the electrolyte solution, the bubbling gas, and the Nafion membrane have been well-purified or cleaned according to the protocol for NRR before each test (details in ESI†).[48–50] 0.05 M H_2SO_4 solution was used as the electrolyte to evaluate the stability and selectivity of the catalyst in the acidic condition so that to determine the industrial feasibility of the catalyst.[51,52] The NH_3 yield and faradaic efficiency (FE) were related to the cathode potential. To determine the optimal cathode potential, the chronoamperometry method was utilized to measure CC-APS 800 at a series of potentials (Fig. 4a). After a reaction time of 2 h, CC-APS 800 with a potential of −0.2 V performed a low NH_3 yield of 5.32×10^{-11} mol s^{-1} cm^{-2} and an FE of 0.47%. Negatively shifting the potential to −0.3 V, CC-APS 800 dramatically demonstrated a maximum NH_3 yield of 9.87×10^{-10} mol s^{-1} cm^{-2} and an FE of 8.11%. CC-APS 800 exhibited the better performance for NRR than those of many other carbon-based catalysts for NRR (Table S2†) as well as the lower preparation cost and less electricity consumption. The performance of CC-APS 800 for NRR declined apparently when the cathode potential further decreased from −0.3 V to −0.5 V. These results were probably attributed to the weaker competitiveness of the NRR process compared to HER process owing to the kinetic limits on the N_2 adsorption and multielectron transfer.[53] In a typical NRR electrolysis, the NH_3–N accumulates almost linearly as the time increases (Fig. S10†).

Following protocols put forward by Andersen *et al.*[54] and Suryanto *et al.*,[55] the isotopic labeling experiment using $^{15}N_2$ gas (^{15}N enrichment of 99 atom%) has been carried out to ensure the genuine capability of the as-synthesized S/N-codoped carbon cloth for NRR (Fig. 5). According to the published literature,[45,54,56] the nitrogen species produced during the NRR process could be distinguished by ^1H NMR spectra due to the chemical shift of triplet coupling of ^{14}N and doublet coupling of ^{15}N. During the isotopic labeling experiment, the as-synthesized S/N-codoped carbon cloth (CC-APS 800) was applied with a potential of −0.3 V *vs.* RHE for 10 h in the electrolyte solution saturated with Ar, $^{15}N_2$ or $^{14}N_2$ gas as the feeding gas, respectively. To remove impurities of reducible, labile nitrogen-containing compounds such as NO_x which is inevitable in the N_2 gas,[57] a Cu impurity trap was introduced, composed of 2 g

Open Access Article. Published on 06 March 2020. Downloaded on 5/9/2026 12:36:21 PM.
This article is licensed under a Creative Commons Attribution-NonCommercial 3.0 Unported Licence.

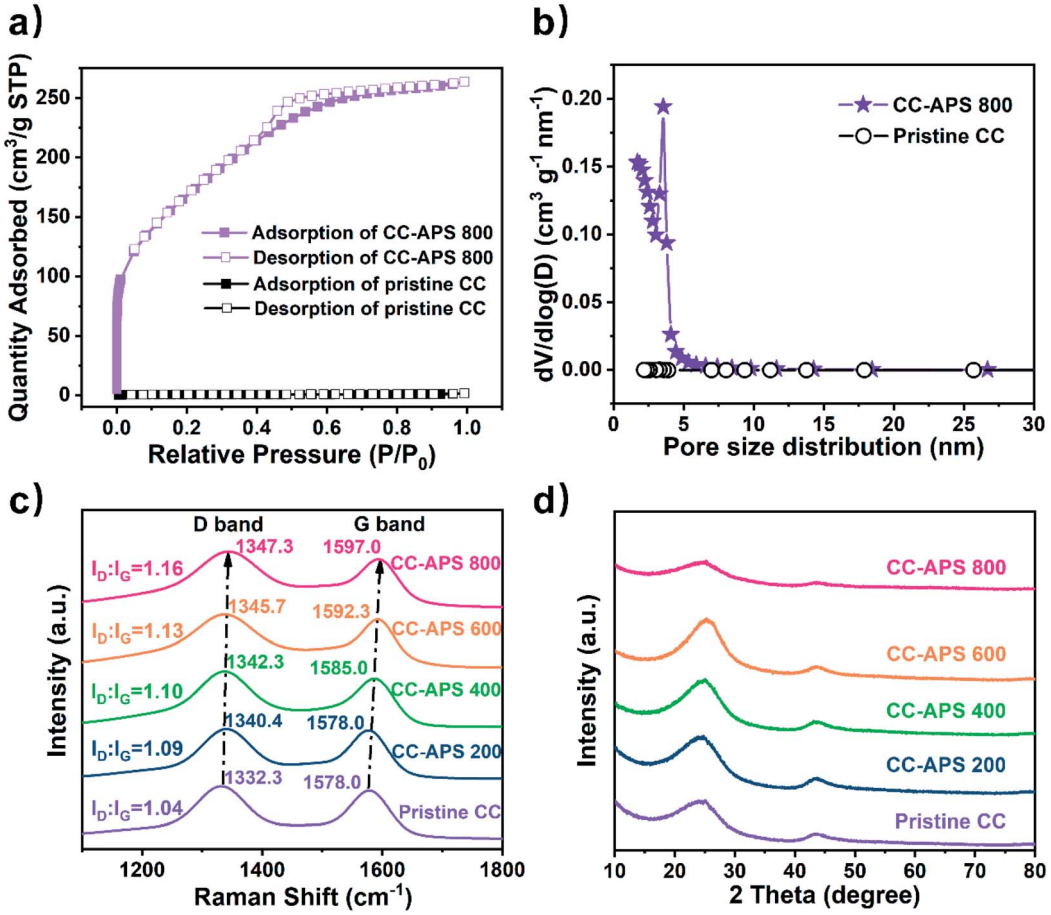

Fig. 3 (a) N_2 adsorption–desorption isotherms and (b) corresponding pore size distributions of the pristine CC and CC-APS 800, respectively. (c) Raman and (d) XRD spectra of the pristine CC, CC-APS 200, CC-APS 400, CC-APS 600, and CC-APS 800.

Cu–Zn–Al oxide catalyst in a U-shaped stainless steel tubing.[58,59] As a result, when using Ar gas as the feeding gas, no peaks of $^{15}NH_4^+$ or $^{14}NH_4^+$ can be observed. It proves that there is no ammonia or other labile N-containing species in the reactor, the electrolyte solution, or the catalysts. However, ^1H NMR spectrum from the experiment with $^{15}N_2$ depicted distinct doublet coupling of ^{15}N in $^{15}NH_4^+$ and weak triplet peaks of ^{14}N in $^{14}NH_4^+$. It revealed that the nitrogen atoms in the synthesized ammonia mainly contributed from the feeding gas of N_2. The small quantity of ^{14}N atoms may come from the background contamination of $^{14}N_2$ in the feeding gas or the breaking of the doped nitrogen in the S/N-codoped carbon cloth.

The durability of CC-APS 800 was also tested by cyclic electrolysis at −0.3 V (details in ESI†). As shown in Fig. 4b, CC-APS 800 exhibited highly reproducible NH_3 yield rates and FEs in 20 h cycles. After the 20 h cycles, the NH_3 yield rate and FE of CC-APS 800 only decreased by 3.4% and 1.4%, respectively. Besides, an uninterrupted electrolysis test of CC-APS 800 for 20 h was also operated (Fig. S11a†). Illegible change in current density was observed after the first durability test, proving the long-time reliability of CC-APS 800. Repeating the NRR test for another 20 h, the current density gradually increased from 5.0 to 5.9 mA cm^{-2} (Fig. S11b†), but the yield rate and FE decreased to 8.36×10^{-10} mol cm^{-2} s^{-1} and 7.36%, respectively (Fig. S12†). The SEM images of the degenerated catalyst (Fig. S13†) revealed negligible change in the surface morphology. It indicates that the passivation of the S/N-codoped carbon cloth may lead from a chemical deactivation rather than the changes in physical structures. Besides, CC-APS 800 after electrolysis performed a very similar Raman spectrum with that of original catalyst (Fig. S14†). After electrolysis in acidic solutions for 40 h, the intensity ratio of the D band and G band (I_D : I_G) of CC-APS 800 decreased very slightly from 1.17 to 1.16, which demonstrated the defects were still abundant in the deactivated catalyst. Furthermore, the XPS spectra of CC-APS 800 after two times durability tests (Fig. S15 and Table S3†) revealed negligible changes in the total S and N content. Even the total content of pyridinic and pyrrolic N is maintained. However, after long-term electrolysis, the ratio of pyridinic N increased to 54.23% in the total N content, while the pyrrolic N decreased to 14.16%. It can be speculated that pyrrolic-N atoms exhibited better performance for NRR than those of pyridinic-N atoms in the N–S co-doped CC. This unique phenomenon has rarely been observed in previous N-doped carbon materials, which may result from the synergistic effect of co-doping of S atoms.

 This journal is © The Royal Society of Chemistry 2020

Open Access Article. Published on 06 March 2020. Downloaded on 5/9/2026 12:36:21 PM.
This article is licensed under a Creative Commons Attribution-NonCommercial 3.0 Unported Licence.

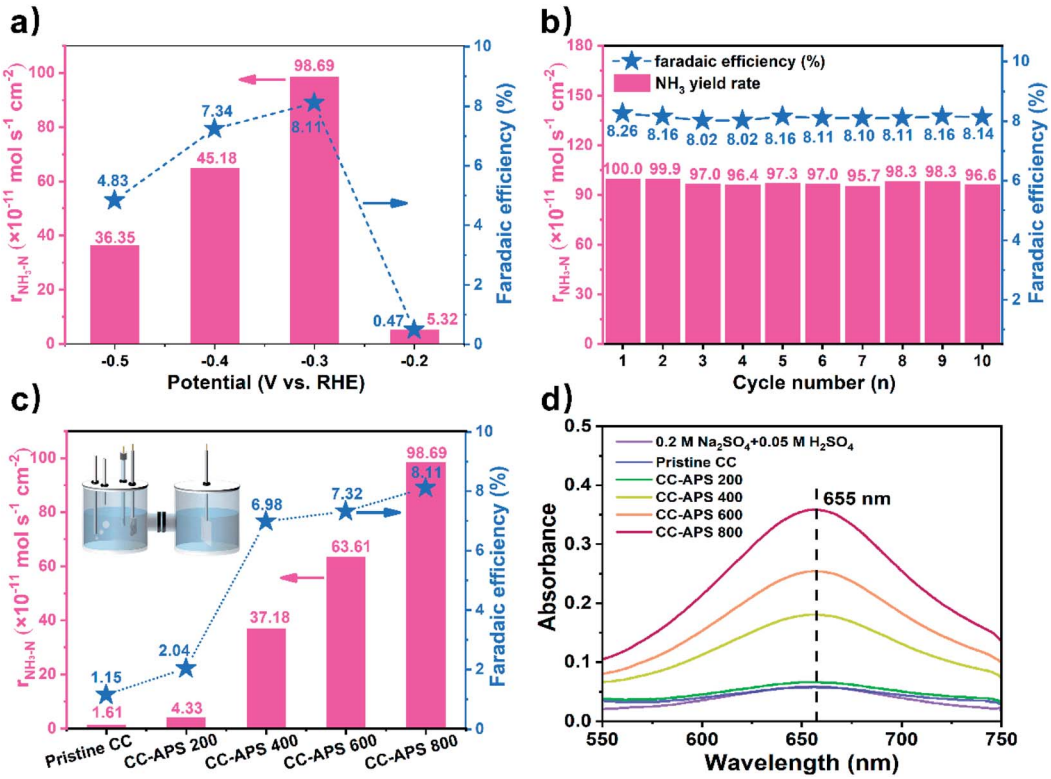

Fig. 4 (a) NH_3 yields and FEs of CC-APS 800 at different potentials. (b) Long-term NRR test of CC-APS 800 at −0.3 V *vs.* RHE for ten cycles (2 h for each cycle). (c) NH_3 yield and FEs of the pristine CC, CC-APS 200, CC-APS 400, CC-APS 600, and CC-APS 800 at −0.3 V *vs.* RHE. (d) UV-vis spectra of N_2-saturated electrolyte stained with indophenol indicator after 2 h NRR test at −0.3 V *vs.* RHE using the pristine CC and CC-APS *X*.

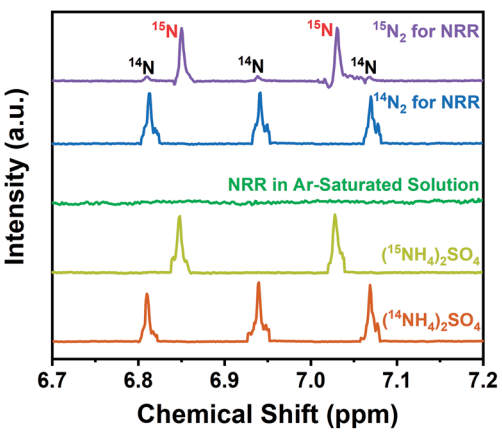

Fig. 5 ^1H NMR spectra of both $^{14}NH_4^+$ and $^{15}NH_4^+$ produced from the NRR using $^{14}N_2$, $^{15}N_2$, and Ar as the feeding gas and using the CC-APS 800 as the electrocatalyst.

Under the same conditions, the NRR performance of the CC-APS *X* was evaluated at −0.3 V *vs.* RHE (Fig. 4c). Because of the lack of defects and active heteroatoms, both the pristine CC and CC-APS 200 exhibit low yield (1.61 and 4.33 × 10^{-11} mol s^{-1} cm^{-2}, respectively) and FE (1.15% and 2.04%, respectively). CC-APS 400 performed an improved NH_3 yield of 3.72 × 10^{-10} mol s^{-1} cm^{-2} and FE of 6.98%. As for CC-APS 600, the NH_3 production and FE have been further enhanced to 6.36 × 10^{-10} mol s^{-1} cm^{-2} and 7.32%, respectively. The change of the NRR performance is consistent with that of S and N content in CC-APS *X*, confirming that the co-doping of S–N heteroatom pairs may enhance the NRR performance of the carbon through a synergistic effect.[60–62] The doping quantity of N in CC-APS 800 is higher than many other N-doped carbon materials prepared through conventional thermochemical methods,[63–65] suggesting that introducing S as a secondary dopant may benefit the co-doping of N in carbon materials.

Fig. 4d displays the UV-vis absorption spectra of the electrolyte incubated by the indophenol blue method after electrolysis at −0.3 V *vs.* RHE for 2 h using different catalysts. The result of the NRR test without any CC catalyst (Fig. 4d, 0.2 M Na_2SO_4 + 0.05 M H_2SO_4) proves that the Pt electrode holder lacks the ability of NRR in experimental conditions. Besides, there is no product in the Ar atmosphere for 2 h (Fig. S16†), which demonstrated that NH_3 was produced exclusively from the electrochemical process with N_2 gas bubbling on the CC-APS 800 electrode. For another comparison, CC treated in the N_2 atmosphere at 800 °C without APS was fabricated, which is signed as CC-800. The XPS spectra of CC-800 (Fig. S17†) displays a weak peak of N 1s and no observable peak of S 2p. The ratio of N/C content is 2.07 at%, which is close to the value of the pristine CC. The result indicates the N_2 gas flow is not an available source for the N doping in CC-APS 800. The low ratio of I_D/I_G (Fig. S18†) and the weak ability of NRR (r = 2.33 ×

Open Access Article. Published on 06 March 2020. Downloaded on 5/9/2026 12:36:21 PM.
This article is licensed under a Creative Commons Attribution-NonCommercial 3.0 Unported Licence.

10^{-11} mol cm^{-2} s^{-1}, FE = 2.05%) proves that N_2 lacks the activity to form defects or introduce N atoms in the CC.

Comparatively speaking, CC-APS 800 displays an FE higher than the pristine CC (1.15%) and defect-rich commercial CC (6.92% (ref. 30)), which even exceeds the N-doped porous carbon (4.2% (ref. 16)), S-doped graphene (7.07% (ref. 66)), and N–P codoped porous carbon (0.075% (ref. 17) and 4.2% (ref. 16)). Some carbon-based catalysts with low dimensions for NRR (graphene, carbon nanotubes, porous carbon nanosheets, carbon nano spikes, *etc.*) may suffer from high preparation costs, weak stability, and high dependency on supporting or binding substances.[67] In contrast, the self-standing CC-APS 800 catalyst displays high mechanical strength but low costs, which is applicable for scaling-up and further commercialization.

A series of electrochemical analysis has been applied to characterize the electrochemical performance of the resultant samples. Electrolysis tests of CC-APS *X* in Ar or N_2 atmosphere were operated to measure the instant electrochemical response to N_2 (Fig. 6a). The current density of CC-APS *X* in the acidic electrolyte solution reflects the mixture reaction of NRR and HER. Once switching the bubbling gas from Ar to N_2, the current density of CC-APS 400, CC-APS 600, and CC-APS 800 ascended quickly by 1.4%, 5.5%, and 6.7%, respectively. CC-APS 800 performs a lower current density of HER than CC-APS 600 (under Ar bubbling), showing the side reaction of HER has been suppressed in CC-APS 800. These results are consistent with the NRR performance of CC-ASP *X* (Fig. 4c), indicating the abundant electrochemical cites for nitrogen reduction on the surface of CC-APS 800. What's more, the linear sweep voltammetry (LSV) curves of CC-APS *X* in N_2 or Ar gas saturated electrolyte have been illustrated in Fig. S19.† A high current density (j = 4.8 mA cm^{-2}) at −0.3 V *vs.* RHE in CC-APS 800 in N_2 saturated condition indicates the robust electroreduction reaction. The LSV curves in the different atmospheres confirmed that CC-APS 800 is electrochemically active over N_2 within a wide potential range.

To further analyze the electrochemical kinetics on CC-APS *X*, electrochemical impedance spectroscopy (EIS) tests have been operated to measure the electrochemical resistances of CC-APS *X* at −0.3 V *vs.* RHE (Fig. 6b). An arc on low and middle frequencies can be observed in the Nyquist plot, reflecting the hybrid electron transfer resistance (R_{ct}) of HER and NRR in CC-APS *X*. Apparently, as the temperature of the heating process increases, the value of R_{ct} inclines from 1902.0 to 17.0 Ω, indicating the electron transfer activity in the resultant sample has been dramatically enhanced. However, the value of R_{ct} rises

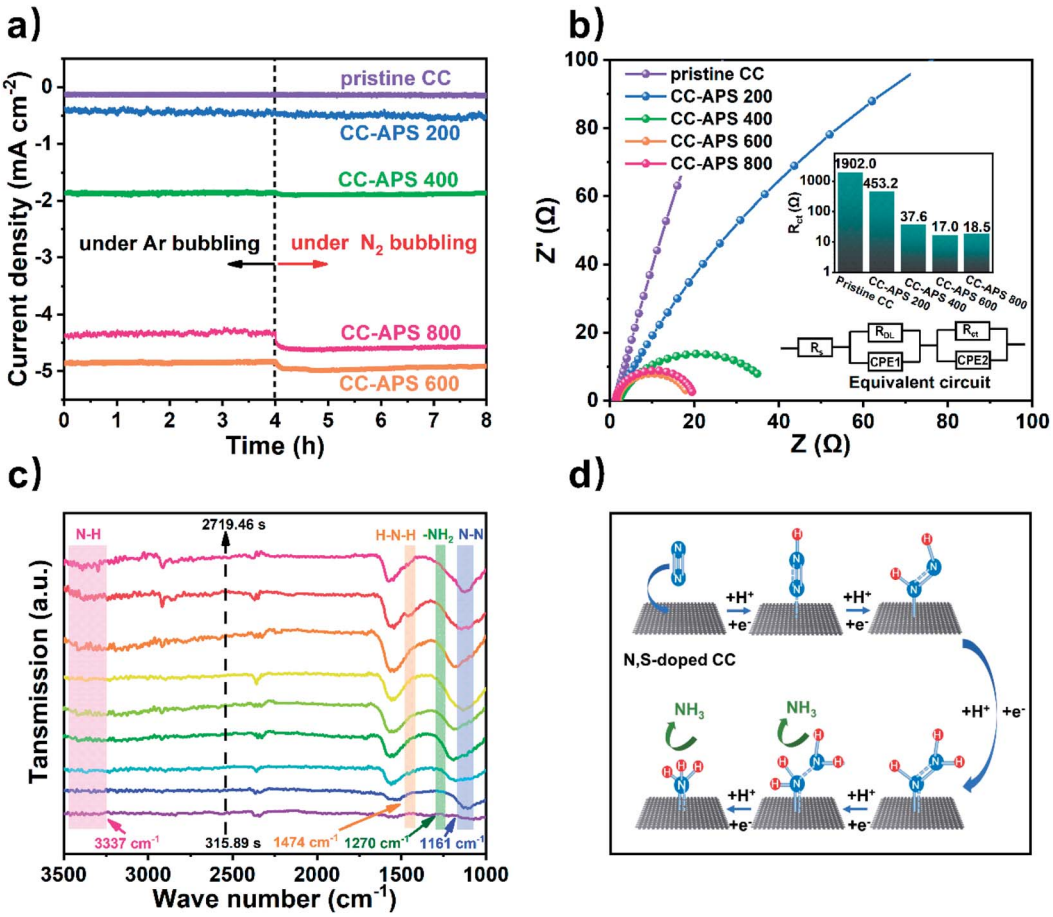

Fig. 6 (a) *I*–*t* curves under −0.3 V *vs.* RHE of the prepared catalyst with Ar or N_2 gas bubbling and (b) the electrochemical impedance spectra under −0.3 V *vs.* RHE in the N_2 saturated electrolyte. (c) The electrochemical *in situ* FTIR spectra on CC-APS 800 in NRR. (d) Associative mechanism of the NRR process on CC-APS 800.

 This journal is © The Royal Society of Chemistry 2020

Open Access Article. Published on 06 March 2020. Downloaded on 5/9/2026 12:36:21 PM.
This article is licensed under a Creative Commons Attribution-NonCommercial 3.0 Unported Licence.

slightly to 18.5 Ω in CC-APS 800. It is because the abundant production of defects and heteroatoms stimulates the NRR but suppresses the dominant HER, and thus heightens the total hybrid resistance of R_{ct}.

Note that N_2H_4 was not detected in the electrolytes after the electrocatalysis of CC-APS *X* (Fig. S20†), implying that CC-APS 800 has excellent selectivity for the NRR. The specific NRR pathway in CC-APS 800 is further investigated by electrochemical *in situ* Fourier transform infrared spectroscopy (*in situ* FTIR). Fig. 6c shows the electrochemical *in situ* FTIR spectra that have been observed on the surface of CC-APS 800 at −0.3 V *vs.* RHE for 2719.46 s in the N_2 saturated electrolyte solution. The absorption at 1161 cm^{-1} is assigned to the N–N stretching, the intensity of which increased with increasing reaction time. Simultaneously, three weak absorptions at 1270, 1474, and 3337 cm^{-1} were observed, which are attributed to $–NH_2$ wagging, H–N–H bending, and N–H stretching of H–N–H bending, respectively.[17] These results verified that N_2H_y ($1 \leq y \leq 4$) species were formed on the surface of CC-APS 800 in the NRR process, suggesting that the production of NH_3 in CC-APS 800 follows an associative mechanism (Fig. 6d). Through this reaction pathway, the N_2 molecules are initially adsorbed on the surface of CC-APS 800. Then, protons get attached to N_2 to weaken the robust N≡N bond and form a –N≡N–H bond. In the third step, another proton further hydrogenates the weakened –N≡N–H bond and forms a –H–N=N–H bond. Thereafter, $–H–N–NH_2$ occurred with the continuous electron transfer and hydrogenation of –H–N=N–H intermediates. Eventually, NH_3 is produced on the surface of CC-APS 800, and the nitrogen is electrochemically fixed under ambient conditions. The technique of *in situ* FTIR is powerful for detecting the transient states in the NRR process, through which the reaction pathway can be revealed directly.[19,20,68] The NRR associated reaction path of S/N-codoped carbon cloth (N≡N → –N≡N–H → –HN=NH → $–HN–NH_2$ → $NH–NH_3$) is consistent with many doped carbon materials in recent reports.[19,20,69]

Conclusion

In this paper, we have firstly prepared an S/N dual-doped carbon cloth catalyst by a novel one-pot thermochemical method. Different from the conventional techniques, S/N elements were facilely introduced into carbon cloth *via* the co-calcination of APS and carbon cloth for the first time. The catalysts with different electrochemical performance can be obtained controllably by adjusting the calcination temperature. The carbon cloth treated with APS at 800 °C (CC-APS 800) exhibited the highest ammonia yield of 9.87×10^{-10} mol s^{-1} cm^{-2} with an excellent faradaic efficiency of 8.11% in 0.05 M H_2SO_4 at the applied potential of −0.3 V *vs.* RHE. As expected, there was no hydrazine formation during the NRR tests. Abundant S/N heteroatoms and the defects on CC-APS 800 were probably as the active and stable electrocatalytic sites for nitrogen reduction to ammonia. Moreover, the electrochemical *in situ* FTIR spectra of CC-APS 800 further revealed a very possible mechanism of the associated hydrogenation pathway for the electro-conversion of N_2 to NH_3. Our work may provide a new guideline for designing metal-free self-supporting electrocatalysts with high efficiency for the NRR and other applications.

Conflicts of interest

The authors declare no competing financial interest.

Acknowledgements

This work was supported by the National Key Research and Development Program of China (2018YFA0901300) and the National Natural Science Foundation of China (No. 51778562).

References

1 B. H. R. Suryanto, H. L. Du, D. B. Wang, J. Chen, A. N. Simonov and D. R. MacFarlane, *Nat. Catal.*, 2019, **2**, 290–296.
2 C. X. Guo, J. R. Ran, A. Vasileff and S. Z. Qiao, *Energy Environ. Sci.*, 2018, **11**, 45–56.
3 J. Y. Zheng, Y. H. Lyu, M. Qiao, R. L. Wang, Y. Y. Zhou, H. Li, C. Chen, Y. F. Li, H. J. Zhou and S. P. Jiang, *Chem*, 2019, **5**, 617–633.
4 Y. Yao, S. q. Zhu, H. j. Wang, H. Li and M. h. Shao, *J. Am. Chem. Soc.*, 2018, **140**, 1496–1501.
5 K. Kugler, M. Luhn, J. A. Schramm, K. Rahimi and M. Wessling, *Phys. Chem. Chem. Phys.*, 2015, **17**, 3768–3782.
6 H. H. Huang, L. Xia, X. F. Shi, A. M. Asiri and X. P. Sun, *Chem. Commun.*, 2018, **54**, 11427–11430.
7 K. Chu, Y. P. Liu, Y. B. Li, H. Zhang and Y. Tian, *J. Mater. Chem. A*, 2019, **9**, 4389–4394.
8 K. Chu, Y. P. Liu, Y. B. Li, J. Wang and H. Zhang, *ACS Appl. Mater. Interfaces*, 2019, **11**, 31806–31815.
9 K. Chu, Y. P. Liu, Y. B. Li, Y. L. Guo, Y. Tian and H. Zhang, *Appl. Catal., B*, 2020, **264**, 31806–31815.
10 R. Zhang, X. Ren, X. F. Shi, F. Y. Xie, B. Z. Zheng, X. D. Guo and X. P. Sun, *ACS Appl. Mater. Interfaces*, 2018, **10**, 28251–28255.
11 L. Zhang, X. Q. Ji, X. Ren, Y. J. Ma, X. F. Shi, Z. Q. Tian, A. M. Asiri, L. Chen, B. Tang and X. P. Sun, *Adv. Mater.*, 2018, **30**, 1800191.
12 R. Zhang, Y. Zhang, X. Ren, Y. L. Luo and X. P. Sun, *ACS Sustainable Chem. Eng.*, 2018, **6**, 9545–9549.
13 X. J. Zhu, Z. C. Liu, Q. Liu, Y. L. Luo, X. F. Shi, A. M. Asiri, Y. P. Wu and X. P. Sun, *Chem. Commun.*, 2018, **54**, 11332–11335.
14 J. P. Paraknowitsch and A. Thomas, *Energy Environ. Sci.*, 2013, **6**, 2839–2855.
15 Y. M. Liu, Y. Su, X. Quan, X. F. Fan, S. Chen, H. T. Yu, H. M. Zhao, Y. B. Zhang and J. J. Zhao, *ACS Catal.*, 2018, **8**, 1186–1191.
16 L. Xia, J. J. Yang, H. B. Wang, R. B. Zhao, H. Y. Chen, W. H. Fang, A. M. Asiri, F. Y. Xie, G. L. Cui and X. P. Sun, *Chem. Commun.*, 2019, **55**, 3371–3374.
17 J. X. Zhao, J. J. Yang, L. Ji, H. B. Wang, H. Y. Chen, Z. G. Niu, Q. Liu, T. S. Li, G. L. Cui and X. P. Sun, *Chem. Commun.*, 2019, **55**, 4266–4269.

Open Access Article. Published on 06 March 2020. Downloaded on 5/9/2026 12:36:21 PM.
This article is licensed under a Creative Commons Attribution-NonCommercial 3.0 Unported Licence.

18 X. M. Yu, P. Han, Z. X. Wei, L. S. Huang, Z. X. Gu, S. J. Peng, J. M. Ma and G. F. Zheng, *Joule*, 2018, **2**, 1610–1622.
19 P. F. Song, H. Wang, L. Kang, B. C. Ran, H. H. Song and R. M. Wang, *Chem. Commun.*, 2019, **55**, 687–690.
20 P. F. Song, L. Kang, H. Wang, R. Guo and R. M. Wang, *ACS Appl. Mater. Interfaces*, 2019, **11**, 12408–12414.
21 C. Chen, D. F. Yan, Y. Wang, Y. Y. Zhou, Y. Q. Zou, Y. F. Li and S. Y. Wang, *Small*, 2019, **15**, 1805029.
22 Y. Kong, Y. Li, B. Yang, Z. J. Li, Y. Yao, J. G. Lu, L. C. Lei, Z. H. Wen, M. H. Shao and Y. Hou, *J. Mater. Chem. A*, 2019, **7**, 26272–26278.
23 J. J. Li, Y. M. Zhang, X. H. Zhang, J. Z. Huang, J. C. Han, Z. H. Zhang, X. J. Han, P. Xu and B. Song, *ACS Appl. Mater. Interfaces*, 2017, **9**, 398–405.
24 K. G. Qu, Y. Zheng, S. Dai and S. Z. Qiao, *Nano Energy*, 2016, **19**, 373–381.
25 K. Qu, Y. Zheng, X. Zhang, K. Davey, S. Dai and S. Z. Qiao, *ACS Nano*, 2017, **11**, 7293–7300.
26 Y. Tian, D. Xu, K. Chu, Z. Wei and W. J. Liu, *J. Mater. Sci.*, 2020, **54**, 9088–9097.
27 X. Chen, Y. Guo, X. Du, Y. Zeng, J. Chu, C. Gong, J. Huang, C. Fan, X. Wang and M. Xiong, *Adv. Energy Mater.*, 2020, **10**, 1903172.
28 I. A. Vorsina and Y. I. Mikhailov, *Russ. Chem. Bull.*, 1996, **45**, 539–542.
29 S. Mukherjee, D. A. Cullen, S. Karakalos, K. Liu, H. Zhang, S. Zhao, H. Xu, K. L. More, G. Wang and G. Wu, *Nano Energy*, 2018, **48**, 217–226.
30 W. Y. Li, T. X. Wu, S. B. Zhang, Y. Y. Liu, C. J. Zhao, G. Q. Liu, G. Z. Wang, H. M. Zhang and H. J. Zhao, *Chem. Commun.*, 2018, **54**, 11188–11191.
31 D. F. Yan, H. Li, C. Chen, Y. Q. Zou and S. Y. Wang, *Small Methods*, 2019, **3**, 1800331.
32 B. B. Huang, X. Hu, Y. C. Liu, W. Qi and Z. L. Xie, *J. Power Sources*, 2019, **413**, 408–417.
33 J. Geng, H. J. Zhang, S. W. Yao, C. L. Cai, Z. F. Ma, J. C. Wang, H. B. Wei and J. H. Yang, *RSC Adv.*, 2019, **9**, 24770–24776.
34 C. J. Zhao, S. B. Zhang, M. M. Han, X. Zhang, Y. Y. Liu, W. Y. Li, C. Chen, G. Z. Wang, H. M. Zhang and H. J. Zhao, *ACS Energy Lett.*, 2019, **4**, 377–383.
35 A. M. El-Sawy, I. M. Mosa, D. Su, C. J. Guild, S. Khalid, R. Joesten, J. F. Rusling and S. L. Suib, *Adv. Energy Mater.*, 2016, **6**, 1501966.
36 Y. Zheng, Y. Jiao, S. Qiao and A. Vasileff, *Angew. Chem., Int. Ed.*, 2017, **130**, 7568–7579.
37 N. Habibi, H. Arandiyan and M. Rezaei, *RSC Adv.*, 2016, **6**, 29576–29585.
38 X. L. Zheng, Y. F. Ji, J. Tang, J. Y. Wang, B. F. Liu, H.-G. Steinrück, K. Lim, Y. Z. Li, M. F. Toney and K. R. Chan, *Nat. Catal.*, 2019, **2**, 55–61.
39 J. Y. Zheng, Y. H. Lyu, M. Qiao, R. L. Wang, Y. Y. Zhou, H. Li, C. Chen, Y. F. Li, H. J. Zhou, S. P. Jiang and S. Y. Wang, *Chem*, 2019, **5**, 617–633.
40 C. C. Li and S. A. Cheng, *Crit. Rev. Biotechnol.*, 2019, **39**, 1015–1030.
41 C. J. Zhao, S. B. Zhang, M. M. Han, X. Zhang, Y. Y. Liu, W. Y. Li, C. Chen, G. Z. Wang, H. M. Zhang and H. J. Zhao, *ACS Energy Lett.*, 2019, **4**, 377–383.
42 L. Xia, X. Wu, Y. Wang, Z. Niu, Q. Liu, T. Li, X. Shi, A. M. Asiri and X. Sun, *Small Methods*, 2019, **3**, 1800251.
43 K. Mamtani, D. Jain, D. Dogu, V. Gustin, S. Gunduz, A. C. Co and U. S. Ozkan, *Appl. Catal., B*, 2018, **220**, 88–97.
44 C. A. Cooper, R. J. Young and M. Halsall, *Composites, Part A*, 2001, **32**, 401–411.
45 A. D. Tan, K. Wan, Y. F. Wang, Z. Y. Fu and Z. X. Liang, *Catal. Sci. Technol.*, 2018, **8**, 335–343.
46 C. D. Lv, Y. M. Qian, C. S. Yan, Y. Ding, Y. Y. Liu, G. Chen and G. H. Yu, *Angew. Chem., Int. Ed.*, 2018, **57**, 10246–10250.
47 X. H. Li, T. S. Li, Y. J. Ma, Q. Wei, W. B. Qiu, H. R. Guo, X. F. Shi, P. Zhang, A. M. Asiri and L. Chen, *Adv. Energy Mater.*, 2018, **8**, 1801357.
48 L. Q. Li, C. Tang, D. Z. Yao, Y. Zheng and S. Z. Qiao, *ACS Energy Lett.*, 2019, **4**, 2111–2116.
49 C. Tang and S. Z. Qiao, *Joule*, 2019, **3**, 1573–1575.
50 C. Tang and S. Z. Qiao, *Chem. Soc. Rev.*, 2019, **48**, 3166–3180.
51 C. J. Van der Ham, M. T. Koper and D. G. Hetterscheid, *Chem. Soc. Rev.*, 2014, **43**, 5183–5191.
52 S. Zhao, D. W. Wang, R. Amal and L. J. Dai, *Adv. Mater.*, 2019, **31**, 1801526.
53 W. S. Zhi, J. Kibsgaard, C. F. Dickens, I. Chorkendorff, J. K. Nørskov and T. F. Jaramillo, *Science*, 2017, **355**, 4998.
54 S. Z. Andersen, V. Čolić, S. Yang, J. A. Schwalbe, A. C. Nielander, J. M. McEnaney, K. Enemark-Rasmussen, J. G. Baker, A. R. Singh and B. A. Rohr, *Nature*, 2019, **570**, 504–508.
55 B. H. Suryanto, H. L. Du, D. B. Wang, J. Chen, A. N. Simonov and D. R. MacFarlane, *Nat. Catal.*, 2019, **2**, 290–296.
56 C. Chen, D. F. Yan, Y. Wang, Y. Y. Zhou, Y. Q. Zou, Y. F. Li and S. Y. Wang, *Small*, 2019, **15**, 1805029.
57 R. Dabundo, M. F. Lehmann, L. Treibergs, C. R. Tobias, M. A. Altabet, P. H. Moisander and J. Granger, *PLoS One*, 2014, **9**, 110335.
58 L. Ma, Y. Cheng, G. Cavataio, R. W. McCabe, L. Fu and J. Li, *Appl. Catal., B*, 2014, **156**, 428–437.
59 L. Ma, Y. S. Cheng, G. Cavataio, R. W. McCabe, L. X. Fu and J. H. Li, *Chem. Eng. J.*, 2013, **225**, 323–330.
60 Y. Tian, D. Z. Xu, K. Chu, Z. Wei and W. M. Liu, *J. Mater. Sci.*, 2019, **54**, 9088–9097.
61 J. C. Li, X. P. Qin, P. X. Hou, M. Cheng, C. Shi, C. Liu, H. M. Cheng and M. H. Shao, *Carbon*, 2019, **147**, 303–311.
62 X. R. Chen, Y. T. Guo, X. C. Du, Y. S. Zeng, J. W. Chu, C. H. Gong, J. W. Huang, C. Fan, X. F. Wang and F. Xiong, *Adv. Energy Mater.*, 2019, **122**, 1903172.
63 X. F. Sima, S. F. Jiang, X. C. Shen and H. Jiang, *Ind. Eng. Chem. Res.*, 2019, **58**, 13868–13878.
64 X. Xin, H. L. Qin, H. P. Cong and S. H. Yu, *Langmuir*, 2018, **34**, 4952–4961.
65 J. J. Wu, C. Wen, X. L. Zou, J. Jimenez, J. Sun, Y. J. Xia, M.-T. Fonseca Rodrigues, S. Vinod, J. Zhong, N. Chopra, I. N. Odeh, G. Q. Ding, J. Lauterbach and P. M. Ajayan, *ACS Catal.*, 2017, **7**, 4497–4503.

 This journal is © The Royal Society of Chemistry 2020

Open Access Article. Published on 06 March 2020. Downloaded on 5/9/2026 12:36:21 PM.
This article is licensed under a Creative Commons Attribution-NonCommercial 3.0 Unported Licence.

66 H. Y. Chen, X. J. Zhu, H. Huang, H. B. Wang, T. Wang, R. B. Zhao, H. G. Zheng, A. M. Asiri, Y. L. Luo and X. P. Sun, *Chem. Commun.*, 2019, **55**, 3152–3155.
67 S. L. Zhao, D. W. Wang, R. Amal and L. M. Dai, *Adv. Mater.*, 2019, **31**, 1801526.
68 P. F. Song, H. Wang, X. M. Cao, N. Liu, Q. Wang and R. M. Wang, *ChemElectroChem*, 2020, **7**, 212–216.
69 C. V. S. Kumar and V. Subramanian, *Phys. Chem. Chem. Phys.*, 2017, **19**, 15377–15387.